Available online at www.sciencedirect.com

SciVerse ScienceDirect

Ceramics International 39 (2013) 2581–2587

CERAMICS INTERNATIONAL

www.elsevier.com/locate/ceramint

Pore structure improvement in cermet for anode-supported protonic ceramic fuel cells

Yu-Eun Park[a], Ho-Il Ji[a], Byung-Kook Kim[a,**], Jong-Ho Lee[a], Hae-Weon Lee[a], Jong-Sung Park[b,*]

[a]*High Temperature Energy Materials Center, Korea Institute of Science and Technology (KIST), Seoul, Republic of Korea*
[b]*Department of Materials Science and Engineering, Myongji University, Yongin 449-728, Republic of Korea*

Received 5 July 2012; received in revised form 8 August 2012; accepted 6 September 2012
Available online 14 September 2012

Abstract

The porous cermet of Yb-doped $BaZrO_3$ and nickel (BZYb–Ni) for anode-supported protonic ceramic fuel cells (PCFCs) was fabricated by compression molding following the liquid condensation process (LCP). The gas permeability of BZYb–Ni produced by LCP (BZYb–Ni_{LCP}) was greater than that of BZYb–Ni produced by a conventional drying method (BZYb–Ni_{CDM}) although their porosities were similar. The greater permeability of BZYb–Ni_{LCP} than that of BZYb–Ni_{CDM} is consistent with more efficient structures for gas flow; a smaller specific surface area, and a larger critical diameter for pores in BZYb–Ni_{LCP} than those for pores in BZYb–Ni_{CDM}.

Keywords: Anode composite; Liquid condensation process; Protonic ceramic; Solid oxide fuel cell

1. Introduction

Solid oxide fuel cells (SOFCs) have numerous advantages, such as high power density, energy efficiency, and fuel flexibility [1]. However, the operating temperatures of SOFCs using an oxygen ion conductor such as yttria-stabilized zirconia (YSZ) is too high (around 800–1000 °C), which usually induces serious chemical or thermo-mechanical degradation of SOFC components during long-term operation. Protonic ceramics, such as rare-earth-doped $BaCeO_3$ (RE-$BaCeO_3$) or $BaZrO_3$ (RE-$BaZrO_3$), have previously been suggested as alternative electrolytes for SOFCs operating at intermediate temperatures [2,3]. In protonic ceramics, a proton is a charge carrier, so the activation energy of ionic conduction in the protonic ceramic is less than that of an oxygen ion conductor. Consequently, ionic conductivities of protonic ceramics are usually higher than those of oxygen ion conductors in an intermediate temperature range, 400–600 °C [2].

In order to reduce the ohmic resistance of an electrolyte for a high-performance SOFC, the electrolyte is usually fabricated as a thin film on a porous anode substrate, usually a ceramic-metal composite (cermet), consisting of an ionic conducting ceramic and a catalytically active metal [4]. Various cermets with nickel and protonic ceramics (such as Y–$BaCeO_3$, Yb–$SrCeO_3$, and Y–$Ba(Ce,Zr)O_3$) have been fabricated as anode cermets for use in protonic ceramic fuel cells by using several methods [5–8]. Starch or graphite powders are usually used as porogens [5,6]. Porous anode cermet structures can also be produced without porogens by sintering at low temperatures [6–8].

A porous anode substrate consists of an anode interlayer and an anode support [9]. The anode interlayer between an electrolyte and an anode support is a thin layer with a thickness of 10–20 μm and a fine pore structure to increase the three-phase boundary (TPB) for anodic reactions [9]. All electrochemical reactions responsible for the activation polarization of anodes mainly occur in the anode interlayer. The anode support, on the other hand, has no electrochemical function. It usually is in the form of a thick substrate with a thickness of 0.5–1.0 mm in order to have sufficient mechanical strength to support a thin electrolyte layer. However, because

*Corresponding author. Tel.: +82 31 330 6467; fax: +82 31 330 6469.
**Corresponding author. Tel.: +82 2 958 6703; fax: +82 2 958 5529.
E-mail addresses: bkkim@kist.re.kr (B.-K. Kim), jspark.phd@mju.ac.kr, jspark.phd@gmail.com (J.-S. Park).

0272-8842/$ - see front matter © 2012 Elsevier Ltd and Techna Group S.r.l. All rights reserved.
http://dx.doi.org/10.1016/j.ceramint.2012.09.020

of the relatively large thickness of the anode support, it should have a high gas permeability to supply reactant gas to or remove product gas from the reaction site while maintaining high electrical conductivity to reduce not only the concentration polarization loss but also the ohmic resistance of the anode support [9]. Concentration polarization loss induced by limited gas diffusion through a porous anode support should be minimized to enhance fuel use in anode-supported SOFCs; therefore, the gas permeability of the anode support is a critical parameter in anode-supported SOFCs and is usually controlled by the morphology and connectivity of the pores.

We previously reported that a more desirable microstructure for anode substrates could be obtained using the liquid condensation process (LCP) instead of the usual spray-dry method to achieve high gas permeability and power density [10]. In LCP, NiO and yttria-stabilized zirconia (YSZ) are mixed with a thermoset polymer in ethanol, which is poured into stirred water; while the ethanol is replaced by water, the thermoset polymer, which is insoluble in water, segregates and solidifies. The dispersed NiO and YSZ are then trapped in the solidified thermoset polymer, producing granules consisting of NiO, YSZ, and thermoset-polymer [10]. Granules produced by LCP have well-dispersed NiO and YSZ without an agglomeration of the same species, which improves the gas permeability of porous anode supports [10]. However, a critical prerequisite for using LCP is that the mixed powder for LCP granulation should be stable in water and CO_2 because a large amount of water is used for granulation and because CO_2 is generated during the burnout of the thermoset polymer. LCP has never been used to produce protonic ceramic because it generally has poor chemical stability in water and CO_2 [11–13]. Nevertheless, among the various protonic ceramics, RE-$BaZrO_3$ has better chemical stability in water vapor and CO_2 than RE-$BaCeO_3$ does, which might be sustained during LCP [11–13].

We thus fabricated an SOFC anode support with Ni and proton-conducting RE-$BaZrO_3$ by using LCP. The anode microstructure was investigated with SEM, and its corresponding micro-structural features (such as volume, size, and shape of constituent phases) were quantitatively analyzed with image analysis. The electrical conductivity and gas permeability of the anode cermet were measured and compared with those of a cermet prepared by the conventional dry method (CDM). The key parameters for achieving high gas permeability are also discussed in terms of the structural features (such as the size, distribution, and connectivity) of pores.

2. Experimental procedure

Yb-doped $BaZrO_3$ composed of $Ba(Zr_{0.85}Yb_{0.15})O_{3-\delta}$ (BZYb) was synthesized using a conventional solid-state reaction. The starting materials were $BaCO_3$ (99.9%, Cerac, USA), ZrO_2 (99%, Junsei, Japan), and Yb_2O_3 (99.9%, high purity, Japan). Precise amounts of the raw powders were mixed using zirconia balls in ethanol for 24 h. The obtained mixture was calcined at 1300 °C for 2 h and then ball-milled again in ethanol for 24 h.

NiO and BZYb composite granules were then prepared with LCP. NiO (0.3 μm, Sumitomo, Japan) and BZYb were mixed with thermoset polymer as a binder and porogen by using zirconia balls for 24 h in ethanol. The ratio of NiO to BZYb to thermoset polymer was 47:40:13 by weight, and the volume ratio of Ni to the total bulk volume in the reduced composite was designed to be around 40 vol%. The mixed slurry was poured into stirred water with a hardening agent to make the granules. The granules obtained from LCP were sieved and dried at room temperature. The dried granules were compacted in a mold heated to 80 °C and were pressed at 100 MPa. The pressed samples were heat-treated at 800 °C to burnout the thermoset polymer and were then sintered at 1450 °C for 10 h.

For comparison, granules consisting of BZYb and NiO without thermoset polymer were prepared using CDM. During CDM, the mixed slurry was dried by heating to around 80 °C. The ratio of NiO to BZYb used in CDM was equal to that used in LCP. The dried powder was pressed at 100 MPa and sintered at 1350 °C for 10 h to produce a composite of BZYb and NiO (BZYb–NiO).

BZYb–NiO composites prepared from LCP and CDM were reduced under a hydrogen atmosphere at 800 °C for 3 h to reduce NiO to Ni. BZYb–NiO_{LCP} and BZYb–NiO_{CDM} represent the sintered composites prepared with LCP and CDM before reduction, and BZYb–Ni_{LCP} and BZYb–Ni_{CDM} represent the reduced composites prepared with LCP and CDM followed by reduction.

Shrinkages at increasing temperatures were measured with a dilatometer (DIL 402C, NETZSCH, Germany). Sintered densities were measured with the Archimedes method by using 2-methoxy ethanol. Crystal structures were investigated with an X-ray diffraction (PW3830, PANalytical, Netherlands). The electrical conductivity of the reduced composites was measured using a DC four-probe method with a current source (KE2425, Keithley, USA) and an electrometer (KE6514, Keithley, USA). The conductivity was measured in the 200–600 °C range, under a wet hydrogen atmosphere.

The flow rates of air through porous composites were measured with a capillary-flow porometer (CFP-1500AEL, PMI, USA) by increasing the differential pressure to 0.6 MPa across the composites. The gas permeabilities of the porous composites were calculated based on the obtained flow rates. The microstructures of the composites were observed with a scanning electron microscope (FEI XL-30 FEG, Philips, Netherlands) and were analyzed with a commercial program used for image analysis (Image-Pro Plus v. 4.5, Media Cybernetics, USA). The volume and size distribution of pores in the composites were measured with a mercury intrusion porosimeter (MIP, AutoPore IV 9500, Micromeritics, USA). During MIP analysis, the intrusion of the mercury into the porous composites was measured under stringently controlled pressures up to 3.5 MPa.

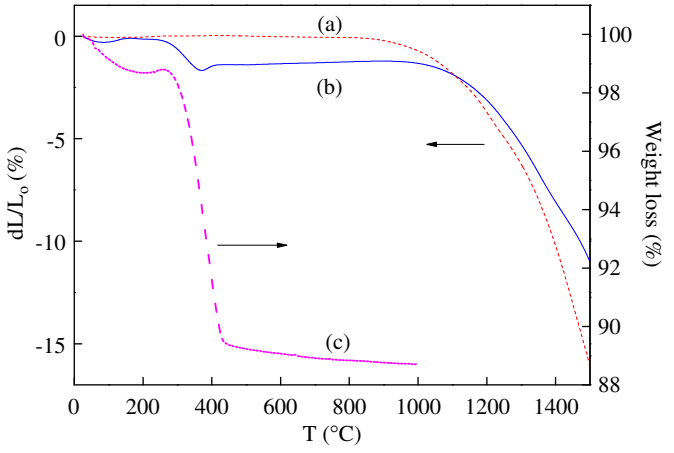

Fig. 1. Dilatometric results for (a) BZYb–NiO$_{CDM}$ and (b) BZYb–NiO$_{LCP}$, including (c) thermal gravimetric result for BZYb–NiO$_{LCP}$.

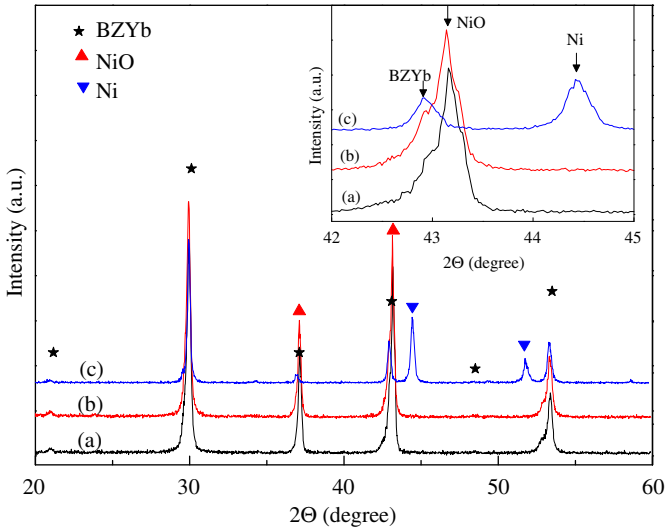

Fig. 2. XRD patterns for BZYb–NiO$_{LCP}$ after (a) LCP, (b) burnout of the thermoset polymer, and (c) reduction.

3. Results and discussion

Fig. 1 shows the dilatometric results for (a) BZYb–NiO$_{CDM}$ and (b) BZYb–NiO$_{LCP}$, including (c) the thermal gravimetric result for BZYb–NiO$_{LCP}$. A weight loss of 11 wt%, due to burnout of the thermoset polymer, was achieved by heating BZYb–NiO$_{LCP}$ to 500 °C. During burnout, BZYb–NiO$_{LCP}$ initially shrank 1.4% up to 500 °C and shrank about 11% overall at 1500 °C. BZYb–NiO$_{CDM}$, on the other hand, shrank more rapidly and shrank 16% overall at 1500 °C. BZYb–NiO$_{LCP}$ shrank less overall than BZYb–NiO$_{CDM}$ did because of the smaller green density achieved by adding the thermoset polymer as a porogen. The green density of BZYb–NiO$_{LCP}$ (about 45%) was actually less than that of BZYb–NiO$_{CDM}$ (55%) after burnout.

The desired porosity of an anode substrate is about 40%, and 41% of the initial volume of NiO will be transferred to the pores during the reduction of NiO to Ni [14]. Thus, a suitable relative density of the BZYb–NiO composite for the porous anode is about 80–90%. In order to satisfy this requirement, BZYb–NiO$_{LCP}$ was sintered at 1450 °C, and its relative density was about 85%, as measured by the Archimedes method. In order to achieve the same density for BZYb–NiO$_{CDM}$ as for BZYb–NiO$_{LCP}$, the former was sintered at 1350 °C, which is 100 °C lower than the sintering temperature for the latter.

Fig. 2 shows the XRD patterns for BZYb–NiO$_{LCP}$ after three sequential steps: (a) LCP, (b) burnout of the thermoset polymer, and (c) reduction. In the XRD patterns of the (a) granules prepared using LCP, there was no unwanted phase, and BZYb did not decompose during LCP despite stirring it in water. Moreover, as shown in Fig. 2(b), BZYb did not decompose into barium carbonate although a large amount of CO_2 was generated during burnout of the thermoset polymer. These results were obtained because the chemical stability of BZYb in water and CO_2 was sufficient and was higher than that of

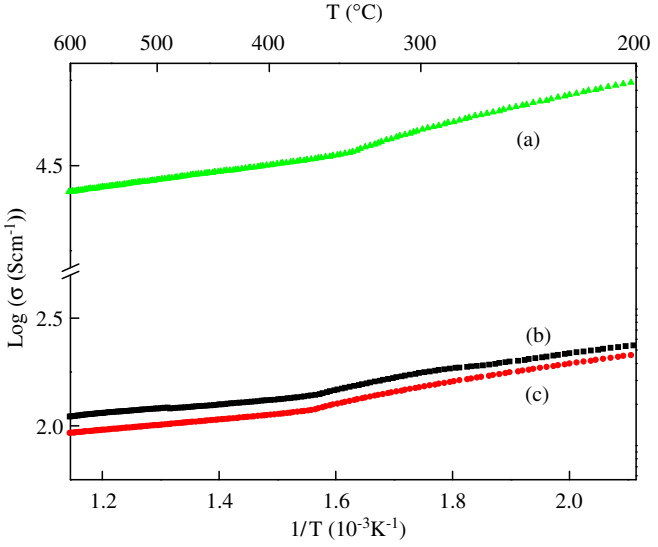

Fig. 3. Electrical conductivities for (a) Ni, (b) BZYb–NiO$_{CDM}$, and (c) BZYb–NiO$_{LCP}$ measured under wet hydrogen atmosphere.

$BaCeO_3$, which usually decomposes into $Ba(OH)_2$ or $BaCO_3$ under high water vapor or a CO_2 atmosphere, respectively. Further, as shown in Fig. 2(c), there was no unwanted phase in either BZYb–Ni$_{LCP}$ or BZYb–Ni$_{CDM}$.

Fig. 3 shows the electrical conductivities of (a) Ni, (b) BZYb–Ni$_{CDM}$, and (c) BZYb–Ni$_{LCP}$, as measured under a wet hydrogen atmosphere. The electrical conductivity of the BZYb–Ni composite increased with decreasing temperature and showed the same tendency as that of the pure nickel. This suggests that the 40 vol% Ni was sufficient to obtain the percolation of nickel particles. The steep change in slope at 357 °C corresponds to the Curie temperature of Ni [15]. The electrical conductivities of BZYb–Ni$_{LCP}$ and BZYb–Ni$_{CDM}$ were similar, which might be due to the similar residual Ni content in the composites.

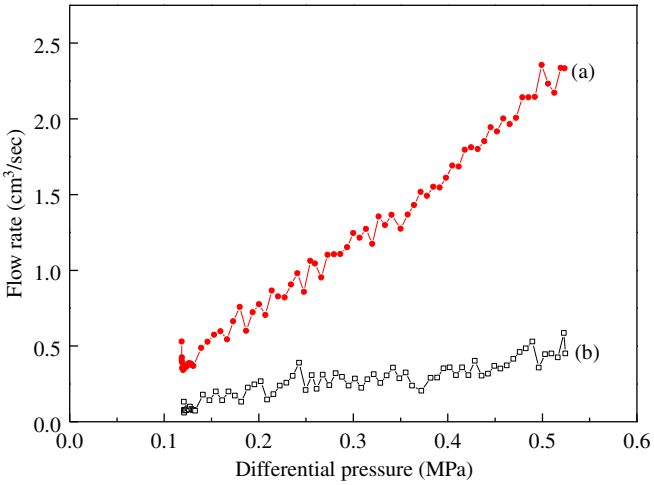

Fig. 4. Permeability test results for BZYb–Ni_{LCP} and BZYb–Ni_{CDM}.

Conductivities around 100 S cm^{-1} at 600 °C for both composites are in the reasonable range of magnitude for the SOFC anode, which correspond to an area-specific resistance (ASR) of 0.001 Ω cm^2 for the 1.0-mm-thick anode support.

Fig. 4 shows the results of the gas-permeability test for BZYb–Ni_{LCP} and BZYb–Ni_{CDM}. A flow rate (Q) can be correlated with a pressure drop (ΔP) across a porous membrane by following Darcy's law:

$$Q = \frac{-kA}{\mu}\frac{\Delta P}{L}, \quad (1)$$

where k, μ, L, and A are the permeability, dynamic viscosity (19 μPa s) for air, thickness of the membrane, and cross-sectional area to a flow, respectively [16]. The gas permeability can be obtained from the slope in Fig. 4 by applying Eq. (1). The gas permeabilities obtained for BZYb–Ni_{LCP} and BZYb–Ni_{CDM} were $1.7\,E^{-15}$ m^2 and $3.6\,E^{-16}$ m^2, respectively. The k value for BZYb–Ni_{LCP} was 4.6 times larger than that for BZYb–Ni_{CDM} although the relative densities of the samples were similar, implying that the pore connectivity of BZYb–Ni_{LCP} was higher than that of BZYb–Ni_{CDM}. This is the key advantage of LCP over CDM because pore connectivity and permeability of an anode support are very important in anode-supported SOFCs. The microstructures of BZYb–Ni_{LCP} and BZYb–Ni_{CDM} were thoroughly analyzed to find the primary factors for the higher gas permeability for BZYb–Ni_{LCP} than for BZYb–Ni_{CDM}.

Figs. 5 and 6 show the back-scattered electron (BSE) images of BZYb–NiO_{LCP}, BZYb–NiO_{CDM}, BZYb–Ni_{LCP}, and BZYb–Ni_{CDM} composites before and after reduction, respectively. In the BSE images of BZYb–NiO_{LCP} and BZYb–NiO_{CDM}, each region of black, gray, and white represents the pores, NiO, and BZYb, respectively. The per area and perimeter per unit area of the pores were measured by image analysis, using three BSE images of BZYb–NiO_{CDM} and BZYb–NiO_{LCP}, respectively. The per area is the ratio of the area of the object to the total area, and the perimeter is the outline length, including the perimeter of the holes. The per

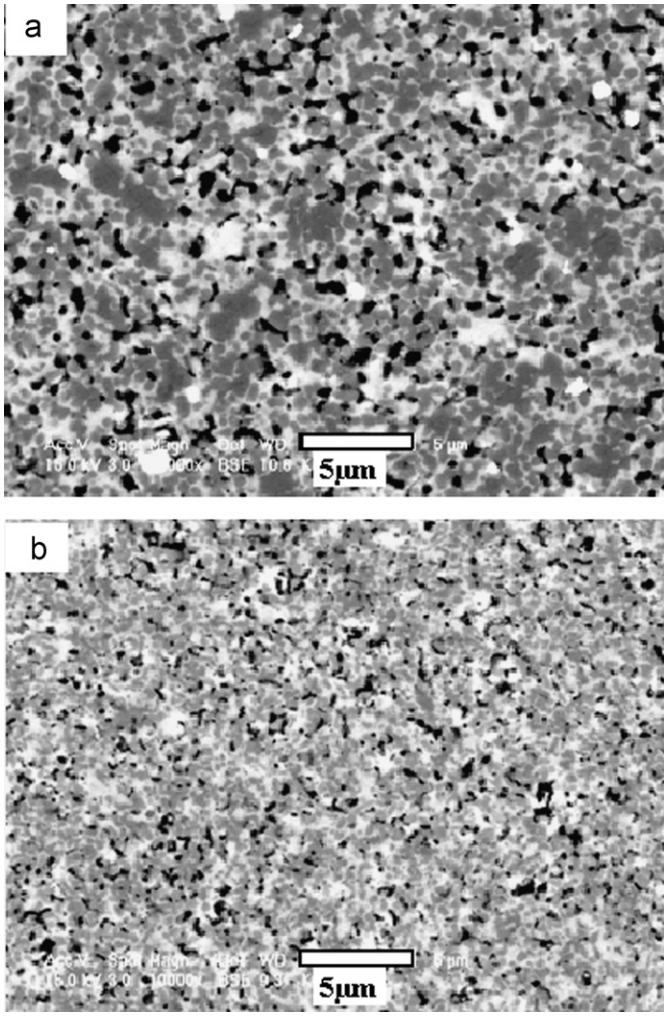

Fig. 5. BSE images of (a) BZYb–NiO_{LCP} and (b) BZYb–NiO_{CDM}.

areas of NiO in BZYb–NiO_{LCP} and BZYb–NiO_{CDM}, measured as 0.54 and 0.51, respectively, were similar. The per areas of BZYb in BZYb–NiO_{LCP} and BZYb–NiO_{CDM} were 0.34 and 0.36, respectively. The similarity in the per areas of both NiO and BZYb in BZYb–NiO_{LCP} and BZYb–NiO_{CDM} can be attributed to the same composition of the composites. However, the pores showed a different behavior in the third constitutional component.

Table 1 lists the image analysis results for pores in the composites produced by LCP and CDM before and after reduction, respectively. Before reduction, the per areas of pores in BZYb–NiO_{LCP} and BZYb–NiO_{CDM} were similar to each other because of the similar sintered densities of the composites. However, the perimeter of the pores in BZYb–NiO_{LCP} was smaller than that of those in BZYb–NiO_{CDM}.

Even after reduction, the per areas of pores in BZYb–Ni_{LCP} and BZYb–Ni_{CDM} were similar to each other even though they had increased to 0.29 and 0.27, respectively, because of the extra pores generated by the reduction of NiO to Ni. However, the perimeter per unit area of the pores in BZYb–Ni_{LCP} (2.27 μm/$μm^2$) was much smaller than that of those in BZYb–Ni_{CDM} (3.50 μm/$μm^2$). We can assume based on fundamental stereological theory that the porosity is

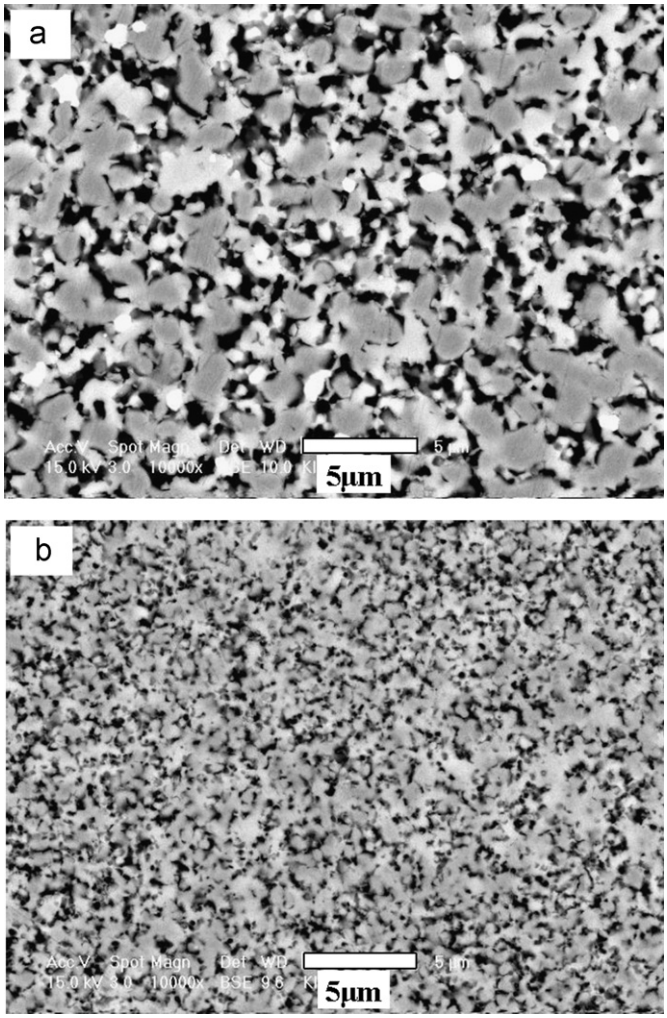

Fig. 6. BSE images of (a) BZYb–Ni$_{LCP}$ and (b) BZYb–Ni$_{CDM}$.

Table 1
Image analysis results for pores in BZYb–Ni$_{LCP}$ and BZYb–Ni$_{CDM}$.

Method		Per-area	Perimeter (μm/μm^2)
Before reduction	LCP	0.12	1.31
	CDM	0.13	2.01
After reduction	LCP	0.29	2.27
	CDM	0.27	3.50

approximately equal to the per area of the pores in the two-dimensional image while the specific surface area of the pores linearly correlates with pore perimeter [17].

Thus, the smaller perimeter of the pores in BZYb–Ni$_{LCP}$ demonstrates that the pores in BZYb–Ni$_{LCP}$ have a smaller specific surface area, which can be very advantageous when gas flows through the pore channel. In a laminar flow regime, there is a thin boundary layer, called the laminar layer, between a surface and a gas. Because of the viscosity of the gas, the gas layer tends to adhere to the surface and resist the flow. Thus, the smaller specific surface area of BZYb–Ni$_{LCP}$ can increase gas permeability by reducing the resistance to the laminar flow of the gas.

In addition to the porosity and specific surface area of pores, another important factor in gas permeability is the tortuosity of the pores. It is well known that the smaller tortuosity of pores can make the greater gas permeability. However, it is difficult to determine the tortuosity of pores by using two-dimensional image analysis although some methods have previously been proposed based on fractal dimension [18]. An alternative method of characterizing three-dimensional pores is mercury intrusion porosimetry (MIP) analysis. In Washburn's equation, the pressure required for mercury to penetrate into pores is inversely proportional to pore size [19]. Thus, by measuring the number of intrusions of mercury with increasing pressure, incremental pore volumes as functions of pore size can be obtained.

Katz and Thompson proposed a theory in which permeability could be estimated from MIP data [19]. From the Katz–Thompson relationship, permeability is related to critical pore diameter (d_c), which can be obtained from MIP data. Because mercury intrudes into smaller pores at higher pressures during MIP, a decrease in pore size corresponds to an increase in measured pressure. Thus in a curve of cumulative pore volume versus pore radius, a rapid increase in pore volume with decreasing pore radius is considered as evidence of the formation of a percolated pathway through a sample, and d_c at that point can be used as a barometer of gas permeability [20,21]. d_c is determined by an inflection point in the curve of cumulative pore volume versus pore radius, where the first derivative of the curve (dV/dP) is a maximum [20].

Fig. 7 shows the pore-size distributions for BZYb–NiO$_{LCP}$, BZYb–NiO$_{CDM}$, BZYb–Ni$_{LCP}$, and BZYb–Ni$_{CDM}$, measured with a mercury intrusion porosimeter: (a) incremental pore volume and (b) cumulative pore volume for each species. The open and closed symbols represent the composites before and after reduction, respectively. Before reduction, the pore size in BZYb–NiO$_{CDM}$ was smaller than that in BZYb–NiO$_{LCP}$ at the maximum incremental pore volume, as shown in Fig. 7(a). After reduction, the incremental pore volumes of both samples increased because of the reduction of NiO to Ni. However, the changes in pore size after reduction were quite different when comparing BZYb–NiO$_{LCP}$ to BZYb–NiO$_{CDM}$. The pore size at the maximum incremental pore volume in BZYb–NiO$_{CDM}$ did not change after reduction while that of BZYb–NiO$_{LCP}$ increased. This represents a smaller connectivity of NiO in BZYb–NiO$_{CDM}$ than in BZYb–NiO$_{LCP}$, considering that NiO, once disconnected from other NiO in composites, cannot produce enlarged pores after reduction of NiO to Ni.

The cumulative pore volumes shown in Fig. 7(b) represent the porosity of each sample. We found that the porosities of BZYb–Ni$_{LCP}$ and BZYb–Ni$_{CDM}$ were similar (about 33% each) while the porosity of BZYb–NiO$_{CDM}$ was slightly higher than that of BZYb–NiO$_{LCP}$. d_c, as shown in Fig. 7(b), was determined by the inflection point in the curve of cumulative pore volume versus the pore radius, as previously mentioned. d_c was 260 nm for BZYb–Ni$_{LCP}$, twice as large as that for BZYb–Ni$_{CDM}$ (110 nm). The larger d_c for BZYb–Ni$_{LCP}$ than for BZYb–Ni$_{CDM}$ can be interpreted as a

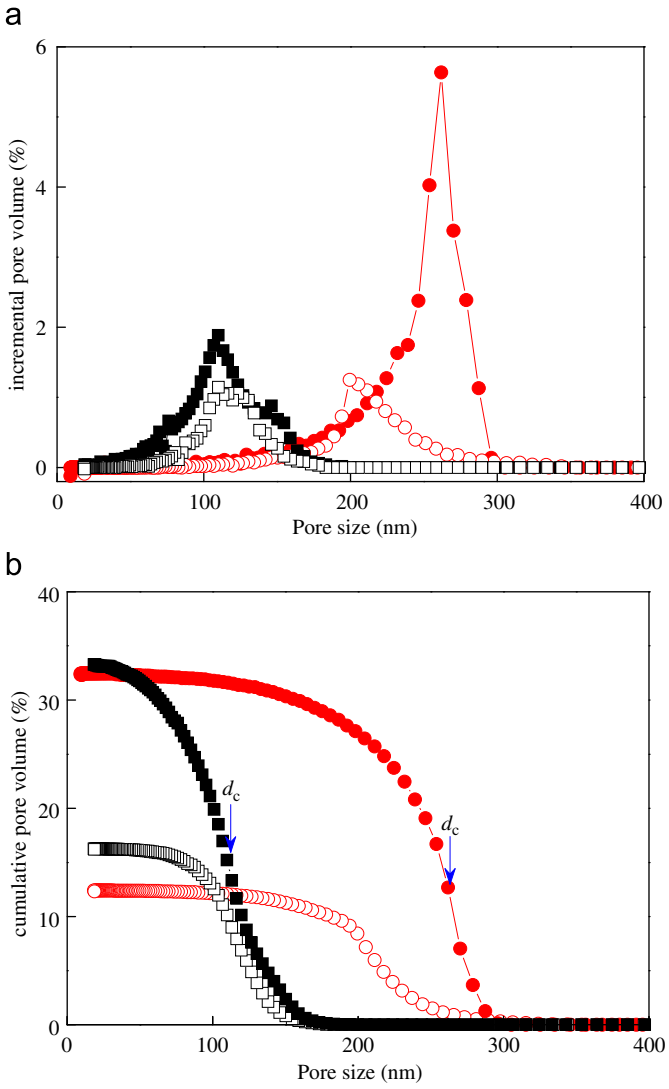

Fig. 7. Pore size distribution for BZYb–NiO_{LCP} (○), BZYb-Ni_{LCP} (●), BZYb–NiO_{CDM} (□) and BZYb-Ni_{CDM} (■) measured with the mercury porosimeter: (a) incremental pore volume and (b) cumulative pore volume.

more efficient path for gas flow through BZYb–Ni_{LCP}, resulting in higher gas permeability for BZYb–Ni_{LCP}.

4. Conclusion

Porous cermets of BZYb and Ni were fabricated as anode substrates for PCFCs by using LCP and CDM. BZYb did not decompose during LCP and a burnout of the thermoset polymer because it had good chemical stability in water and CO_2. The electrical conductivities of BZYb–Ni_{LCP} and BZYb–Ni_{CDM} were similar and sufficiently high for using these cermets as anode supports.

The gas permeability of BZYb–Ni_{LCP} was about five times higher than that of BZYb–Ni_{CDM}, while their porosities were similar. SEM images showed that the perimeters of the pores in BZYb–Ni_{LCP}, proportional to the specific surface area of pores in a 3-dimensional structure, were smaller than those in BZYb–Ni_{CDM}. The mercury intrusion porosimetry data showed that the critical pore diameter in BZYb–Ni_{LCP} was larger than that in BZYb–Ni_{CDM}, while the porosity of BZYb–Ni_{LCP} was nearly equal to that of BZYb–Ni_{CDM}.

The smaller specific surface area and larger critical diameter of pores in BZYb–Ni_{LCP} represent less resistance in laminar flow and a more efficient path for gas flow, resulting in a higher permeability for BZYb–Ni_{LCP} than for BZYb–Ni_{CDM}. Our future work will compare other requirements, such as electrochemical properties and power generation, for cermets produced by LCP and CDM.

Acknowledgments

This work was supported by the Fusion Research Program for Green Technologies through the National Research Foundation of Korea (NRF) funded by the Ministry of Education, Science, and Technology (2012-0006186) and was also supported by the 2012 Research Fund of Myongji University in Korea.

References

[1] S.P.S. Badwal, K. Foger, Solid oxide electrolyte fuel cell review, Ceramics International 22 (3) (1996) 257–265.
[2] L. Chevallier, M. Zunic, V. Esposito, E. Di Bartolomeo, E. Traversa, A wet-chemical route for the preparation of Ni–$BaCe_{0.9}Y_{0.1}O_{3-\delta}$ cermet anodes for IT-SOFCs, Solid State Ionics 180 (9–10) (2009) 715–720.
[3] T. Delahaye, O. Joubert, M.T. Caldes, Y. Piffard, P. Stevens, Synthesis and characterization of a Ni/$Ba_2In_{0.6}Ti_{1.4}O_{5.7}\Delta_{0.3}$ cermet for SOFC application, Solid State Ionics 177 (33–34) (2006) 2945–2950.
[4] H.P. Ding, B. Lin, X.Q. Liu, G.Y. Meng, High performance protonic ceramic membrane fuel cells (PCMFCs) with $Ba_{0.5}Sr_{0.5}Zn_{0.2}Fe_{0.8}O_{3-\delta}$ perovskite cathode, Electrochemistry Communications 10 (9) (2008) 1388–1391.
[5] A.S. Eldieb, R.D. Hooton, Evaluation of the Katz–Thompson model for estimating the water permeability of cement-based materials from mercury intrusion porosimetry data, Cement Concrete Research 24 (3) (1994) 443–455.
[6] H. Iwahara, Y. Asakura, K. Katahira, M. Tanaka, Prospect of hydrogen technology using proton-conducting ceramics, Solid State Ionics 168 (3–4) (2004) 299–310.
[7] A.J. Katz, A.H. Thompson, Prediction of rock electrical-conductivity from mercury injection measurements, Journal of Geophysical Research Solid 92 (B1) (1987) 599–607.
[8] K.D. Kreuer, Aspects of the formation and mobility of protonic charge carriers and the stability of perovskite-type oxides, Solid State Ionics 125 (1–4) (1999) 285–302.
[9] K.D. Kreuer, Proton-conducting oxides, Annual Review of Materials Research 33 (2003) 333–359.
[10] J.H. Lee, J.W. Heo, D.S. Lee, J. Kim, G.H. Kim, H.W. Lee, H.S. Song, J.H. Moon, The impact of anode microstructure on the power generating characteristics of SOFC, Solid State Ionics 158 (3–4) (2003) 225–232.
[11] J.H. Lee, H. Moon, H.W. Lee, J. Kim, J.D. Kim, K.H. Yoon, Quantitative analysis of microstructure and its related electrical property of SOFC anode, Ni–YSZ cermet, Solid State Ionics 148 (1–2) (2002) 15–26.
[12] G. Liu, H. Yu, Stereological characterization of particle contiguity, Journal of Microscopy-Oxford 181 (1996) 82–87.
[13] G.C. Mather, F.M. Figueiredo, D.P. Fagg, T. Norby, J.R. Jurado, J.R. Frade, Synthesis and characterisation of Ni–$SrCe_{0.9}Yb_{0.1}O_{3-\delta}$ cermet anodes for protonic ceramic fuel cells, Solid State Ionics 158 (3–4) (2003) 333–342.

[14] H. Matsumoto, Y. Kawasaki, N. Ito, M. Enoki, T. Ishihara, Relation between electrical conductivity and chemical stability of $BaCeO_3$-based proton conductors with different trivalent dopants, Electrochemical and Solid State 10 (4) (2007) B77–B80.
[15] H. Matsumoto, I. Nomura, S. Okada, T. Ishihara, Intermediate-temperature solid oxide fuel cells using perovskite-type oxide based on barium cerate, Solid State Ionics 179 (27–32) (2008) 1486–1489.
[16] H. Darcy, Les fontaines publiques de la ville de dijon (The public fountains of the town of dijon), Dalmont, Paris, 1856.
[17] J.S. Park, J.H. Lee, H.W. Lee, B.K. Kim, Low temperature sintering of $BaZrO_3$-based proton conductors for intermediate temperature solid oxide fuel cells, Solid State Ionics 181 (3–4) (2010) 163–167.
[18] B.M. Yu, Analysis of flow in fractal porous media, Applied Mechanics Reviews 61 (5) (2008) 050801–050819.
[19] E.W. Washburn, The Dynamics of Capillary Flow, Physical Review 17 (3) (1921) 273–283.
[20] F. Zhao, A.V. Virkar, Dependence of polarization in anode-supported solid oxide fuel cells on various cell parameters, Journal of Power Sources 141 (1) (2005) 79–95.
[21] W.Z. Zhu, S.C. Deevi, A review on the status of anode materials for solid oxide fuel cells, Materials Science and Engineering A: Structural Materials 362 (1–2) (2003) 228–239.